

# Chapter 7

## Theoretical Studies of Plasmonic Effects in Organic Solar Cells

Wei E. I. Sha, Wallace C. H. Choy and Weng Cho Chew

**Abstract** The book chapter provides a systematic study on plasmonic effects in organic solar cells (OSCs). We first introduce the concepts, significance, and recent progress of OSCs incorporating plasmonic nanostructures. On the basis of unique features of OSCs, we exploit versatile resonance mechanisms acting on the absorption enhancement of OSCs; for example, Fabry-Pérot mode, quasi-guided mode, and plasmonic mode. Next, we present rigorous theoretical models to characterize optical properties of OSCs. The key physical quantities, as well as the pros and cons of different models, are described in detail. After that, we show some theoretical results to unveil the fundamental and device physics of plasmonic effects in typical OSC structures. Finally, we conclude the chapter and identify future opportunities in this field.

---

W. E. I. Sha (✉) · W. C. H. Choy · W. C. Chew  
Department of Electrical and Electronic Engineering, The University of Hong Kong,  
Pokfulam Road, Hong Kong, People's Republic of China  
e-mail: wsha@eee.hku.hk

W. C. H. Choy  
e-mail: chchoy@eee.hku.hk

W. C. Chew  
e-mail: wcchew@hku.hk

W. C. Chew  
Department of Electrical and Computer Engineering, University of Illinois,  
Urbana-Champaign, USA

## 7.1 Introduction

Organic solar cells (OSCs) [1–3] have drawn much attentions in recent years, due to their interesting properties in terms of light incoupling and photocurrent generation, as well as the prospect of large-area production and low-cost processing. Many organic semiconductors exhibit very high absorption coefficients, making them promising for photovoltaic devices. However, short lifetime and diffusion length of exciton result in ultrathin-active-layer configuration in OSCs with a typical thickness of a few hundreds nanometers. The configuration limits the light absorption efficiency, and thereby the power conversion efficiency of OSCs. Having unique features of tunable resonance and unprecedented near-field concentration, plasmon is an enabling technique for light manipulation and management [4–6]. By altering the metallic nanostructure, the properties of plasmons, in particular their interactions with light, can be tailored, which offers the potential for developing new types of optoelectronic devices. Meanwhile, the use of metallic materials with negative permittivity is one of the most feasible ways of circumventing the fundamental (half-wavelength) limit and achieving localization of electromagnetic energy (at optical frequencies) into nanoscale. Breaking the half-wavelength limit has a fundamental significance for the optical design of thin-film OSCs.

Plasmonic effects allow us to significantly improve the optical absorption of thin-film OSCs [7] and promote emerging solar cell technology meeting clean energy demands. So far, plasmonic nanostructures can offer three principles to enhance the optical absorption of OSCs. The first one is surface plasmon resonance by metallic gratings fabricated on the top or bottom of the active layer [8–17]. The second one is local plasmon resonance by metallic nanoparticles incorporated into or near the active layer [18–30]. The third one is plasmon coupling and hybridization, such as surface plasmon resonance coupled with local plasmon resonance or plasmon resonance coupled with photonic resonance [31–33].

## 7.2 Resonance Mechanisms

Critically different from the thin-film polycrystalline or amorphous silicon SCs with active layer thickness of a few microns [34], the active polymer layer of thin-film OSCs only has a few hundreds nanometers or even thinner thickness due to an extreme short exciton diffusion length [1]. Such thin active layer with low refractive index induces not only the weak optical absorption of OSCs but also fundamental (half-wavelength) limit of the optical design. On the one hand, the strong Fabry-Pérot mode (or waveguide mode) cannot be expected in the ultrathin active layer. On the other hand, the physical mechanism of near-field concentration (not far-field scattering) should be taken into account in the design. Taking full advantage of versatile resonance mechanics is essential to enhance the optical

absorption of OSCs. Noting that the obscure and disparate glossaries describing the same resonance mechanism, we will focus more on their physical understandings and unique features.

**Fabry-Pérot mode.** The planar multilayer device can support the Fabry-Pérot mode whose spectrum has symmetric Lorentzian line shape. Considering the plane-wave excitation in OSC problems, the eigenmode of the multilayer device cannot be excited due to the momentum or phase mismatch ( $\beta > k_0$ ). The Fabry-Pérot mode can be understood by the mode coupling between the excitation solution and the eigenmode. The fundamental limit in the optical design of OSCs forbids the Fabry-Pérot mode bouncing in a single active layer but possibly in several layers. Compared to thicker amorphous silicon SCs, OSCs support weaker Fabry-Pérot mode. The nonplanar device structure can also support the Fabry-Pérot mode if the nonplanar structure can be approximately decomposed as multiple planar structures [15].

**Quasi-guided mode.** The space harmonics in periodic nanostructure provide additional momentum, so that the eigenmode or guided mode can be excited with the momentum matching condition of  $\pm\text{Re}(\beta) = k_0 \sin \theta + \frac{2\pi}{P}m$ ,  $m = 0, \pm 1, \pm 2, \dots$ . Here, we consider a 1-dimensional periodic structure with a periodicity  $P$  and an incident angle  $\theta$ . The complex propagation constant  $\beta$  implies that the excited guided mode cannot be perfectly trapped in the grating layer but giving rise to a leaky wave. Arising from the constructive and destructive interference of a narrow discrete guided mode with a broad continuum (incident light), the quasi-guided mode [35] with an asymmetric and narrow Fano line shape has extraordinary transmittance and reflectance called Wood's anomaly [36–38]. The pronounced quasi-guided mode enhances the absorption of OSCs; however, its performance is limited by the narrow bandwidth.

**Plasmonic mode.** The excitation of plasmons by light is denoted as a surface plasmon resonance (SPR) for planar surfaces or localized plasmon resonance (LPR) for nanometer-sized metallic structures [39–41]. SPRs are electromagnetic excitations propagating at the interface between a dielectric and a metal, evanescently confined in the perpendicular direction. Using light to excite the SPR, the momentum matching condition can be satisfied by using a periodic structure with space harmonics or a subscatterer producing evanescent waves. LPRs are nonpropagating excitations of the conduction electrons of metallic nanostructures coupled to the electromagnetic field. The curved surface of the particle exerts an effective restoring force on the driven electrons, so that a resonance can arise at a specific wavelength independent of wave vector. The half-wavelength limit in the optical design of OSCs compels researchers to pay more attention on the physical mechanism of near-field concentration (not far-field scattering). Hence, plasmonic mode, which has unique features of near-field enhancement, is one of the best candidates to boost the optical absorption of OSCs. The resonance peaks of plasmonic mode strongly depend on the material, geometry, and surrounding environment and can be highly tunable and manipulated.

**Mode hybridization.** The superradiant plasmonic mode oscillating in-phase can be realized by the mode coupling and hybridization mechanisms [42, 43], which occur in the close-packed metallic nanostructures. For example, longitudinal modes in the metallic nanosphere chain or symmetric modes in two coupled metallic plates can increase the optical absorption of OSCs by several folds [30, 33]. Likewise, the LPR by a metallic nanosphere interacted with the SPR by a metallic plate leads to coherent near-field enhancement [33]. Moreover, the plasmonic mode can couple to the Fabry-Pérot mode through carefully optimizing both device and metallic structures [31, 32]. Mode coupling and hybridization open up a more effective and hopeful way in the optical design of OSCs.

**Intrinsic limit and beyond.** The intrinsic limit of plasmonic effects is the bad spectral overlap between the absorption of active materials and plasmonic resonances. In other words, strong plasmonic resonances only appear in the weak absorption region of active materials. For example, the absorption peak of the active material P3HT:PCBM is around 500 nm; however, the embedded into P3HT:PCBM are respectively at 600 and 650 nm. There are two potential schemes to go beyond the limit. One is to employ large and lossless dielectric concentrators [44–46]. Nevertheless, embedding too large dielectric scatterers seems not to be practical in fabricating thin-film OSCs. Exploring the mode hybridization mechanism is an alternative way to overcome the difficulty. By tuning the thicknesses of active and spacer layers, plasmon-coupled Fabry-Pérot mode can overlap with the absorption peak of active materials [16]. Symmetry breaking and retardation effects allow us to excite the dark modes or high-order modes in the vicinity of metallic structures with broadband and strong resonances [47].

## 7.3 Theoretical Model

### 7.3.1 Comparisons of Various Models

Computational electromagnetics [48], which are used for modeling the interaction of electromagnetic fields with physical objects and surrounding environment, play an important role in characterizing and optimizing the optical design of OSCs. A rigorous, fast, and efficient solution to Maxwell's equations facilitates understanding the underlying device physics, reducing the experimental cost, and accelerating the research and development period. With the aid of state-of-the-art methods, the critical physical quantities in the optical design of OSCs, such as optical absorption of active material, can be illustrated for observation and analyzed for optimization. It is highly desirable to know the strengths and weaknesses of various theoretical methods in modeling the optical properties of OSCs.

**Time-domain methods versus frequency-domain methods.** Most optical materials are dispersive, therefore, a recursive convolution method [49] or a piecewise linear recursive convolution method [50] must be adopted for time-domain

methods. For noble metals with plasmonic effects in the visible light range, such as silver and gold, the complex refractive index has to be described by a large number of summation terms in the Lorentz-Drude model [51] leading to longer calculation time. However, for frequency-domain methods, one can directly employ an experimentally tabulated refractive index of the dispersive materials. Another difficulty in time-domain methods is to treat the periodic boundary condition particularly for the oblique incidence caused by the anticausal property of the Floquet theorem. In most places, unless a solar panel is mounted on an expensive tracking system, most of the time, light is incident on the array obliquely. Hence, the ability of frequency-domain methods to handle the case of oblique incidence is clearly an important advantage over time-domain methods [52]. Moreover, time-domain methods suffer from numerical dispersion and stability problems in contrast to frequency-domain methods [53, 54]. This drawback becomes more serious if a 3-dimensional large-scale SC structure is investigated. A significant merit associated with time-domain method is a broadband simulation in the solar spectrum of interest. The frequency-domain method can employ the parallel computing technique to circumvent the problem.

**Integral equation methods versus differential equation methods.** Differential equation methods involving finite-difference and finite-element algorithms [54, 55] can treat a variety of inhomogeneous boundary conditions conveniently. The methods have a powerful ability to model the complex device structure of OSCs incorporating the metallic gratings or nanoparticles. The produced matrix by the differential equation methods is sparse due to the “local” differential operators of Maxwell’s equations or wave equations. The method consumes memory cost of  $O(N)$  and complexity of  $O(N)$  per matrix–vector multiplication in Krylov subspace iteration algorithm [55, 56]. Moreover, multifrontal or multigrid methods [57, 58] can speed up the solution process of the differential equations. To simulate the interaction between light and OSCs, an efficient absorption boundary condition, as well as additional volume grids enclosing the OSC device, has to be adopted.

In comparison with differential equation methods, integral equation methods [56, 59] connect field components to equivalent currents by using “global” integral operators represented with the dyadic Green’s functions. As a result, integral equation methods always guarantee higher accuracy but lead to full dense matrix. Fortunately, matrix-free fast algorithms [60], such as fast Fourier transform (FFT) [61, 62] and fast multipole methods [63, 64], can significantly reduce the computer resources occupied by the dense matrix. Thanks to the Green’s tensor, the integral equation methods automatically satisfy the radiation boundary condition but need singularity treatments. In particular, the surface integral equation method having a unique feature of surface triangulation produces much smaller unknowns. However, the method can only be employed to analyze a homogenous or piecewise-homogenous structure. For an arbitrary inhomogeneity or complex environment encountered in plasmonic nanodevices, the near-field calculation by the SIE method is hard to implement.

**Mode-matching methods.** Mode-matching method [59, 65] is a commonly used technique for the formulation of optical problems, especially for structures

consisting of two or more separated regions. It is based on expanding the fields and matching them at the boundaries of different regions, and thus lends itself naturally to the analysis of multilayer optical devices. The most representative of mode-matching methods involves rigorous coupled-wave analysis [66], scattering-matrix method [67], and plane wave expansion method [68]. Using cheap computer resources, these methods are specially useful in characterizing the optical response of periodic OSC devices. The zero-order and high-order transmittance and reflectance can be easily obtained with a program. However, it is not well suited for characterizing plasmonic effects, because a large quantity of modes are required to describe the plasmon coupling and hybridization. For mode-matching methods, computing the optical absorption of active materials for the metal-incorporated OSCs is nontrivial. The trivial absorbance cannot truly represent the optical absorption of OSCs, and electric fields should be postprocessed for excluding the metallic absorption. Additionally, cascading many layer media with repeated matrix multiplications will cause the stability and accuracy issues, which always happens in OSC modeling with the curved geometries.

### 7.3.2 Finite-Difference Frequency-Domain Method

Considering a 2-dimensional OSC structure, the Maxwell's equations can be decoupled into a TE and TM modes. The wave equations for TE and TM modes are respectively formulated as [59]

$$\frac{1}{\varepsilon_r} \frac{\partial}{\partial x} \left( \frac{1}{\mu_r} \frac{\partial E_z}{\partial x} \right) + \frac{1}{\varepsilon_r} \frac{\partial}{\partial y} \left( \frac{1}{\mu_r} \frac{\partial E_z}{\partial y} \right) + k_0^2 E_z = 0 \quad (7.1)$$

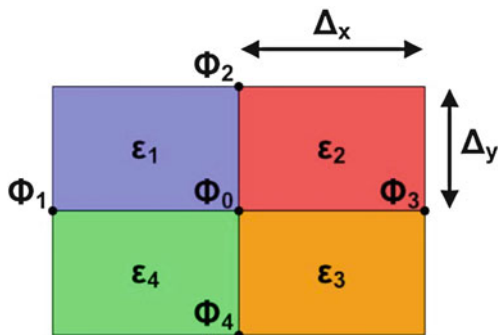
$$\frac{1}{\mu_r} \frac{\partial}{\partial x} \left( \frac{1}{\varepsilon_r} \frac{\partial H_z}{\partial x} \right) + \frac{1}{\mu_r} \frac{\partial}{\partial y} \left( \frac{1}{\varepsilon_r} \frac{\partial H_z}{\partial y} \right) + k_0^2 H_z = 0 \quad (7.2)$$

where  $k_0$  is the wave number of incident light, and  $\varepsilon_r$  and  $\mu_r$  are the relative permittivities and permeabilities, respectively. Regarding nonmagnetic optical materials,  $\mu_r = 1$ ,  $\varepsilon_r = n_c^2$ , and  $n_c$  is the complex refractive index of optical materials.

With the Yee lattice [69], the 2D finite-difference frequency-domain (FDFD) method is utilized to characterize the optical properties of OSCs. As shown in Fig. 7.1, the five-point stencil is adopted for the FDFD method. The discretized forms for the TE and TM wave equations are respectively of the form

$$2 \left( \frac{1}{\Delta_x^2} + \frac{1}{\Delta_y^2} \right) \frac{\Phi_0}{\bar{\varepsilon}} - k_0^2 \Phi_0 - \frac{\Phi_1 + \Phi_3}{\bar{\varepsilon} \Delta_x^2} - \frac{\Phi_2 + \Phi_4}{\bar{\varepsilon} \Delta_y^2} = 0, \quad \Phi = E_z \quad (7.3)$$

**Fig. 7.1** The five-point stencil for the FDFD method.  $\Delta_x$  and  $\Delta_y$  are respectively the spatial steps along the  $x$  and  $y$  directions.  $\Phi = E_z$  for the TE polarization and  $\Phi = H_z$  for the TM polarization. Here,  $\varepsilon = n_c^2$  is the relative permittivity in the discretized region and  $n_c$  is the complex refractive index of the optical material



$$2 \left( \frac{1}{\Delta_x^2} + \frac{1}{\Delta_y^2} \right) \frac{\Phi_0}{\bar{\varepsilon}} - k_0^2 \Phi_0 - \frac{\varepsilon_1^{-1} + \varepsilon_4^{-1}}{2\Delta_x^2} \Phi_1 - \frac{\varepsilon_2^{-1} + \varepsilon_3^{-1}}{2\Delta_x^2} \Phi_3 - \frac{\varepsilon_1^{-1} + \varepsilon_2^{-1}}{2\Delta_y^2} \Phi_2 - \frac{\varepsilon_3^{-1} + \varepsilon_4^{-1}}{2\Delta_y^2} \Phi_4 = 0, \quad \Phi = H_z \quad (7.4)$$

$$\bar{\varepsilon} = \begin{cases} \frac{\varepsilon_1 + \varepsilon_2 + \varepsilon_3 + \varepsilon_4}{4}, & \Phi = E_z \\ 4(\varepsilon_1^{-1} + \varepsilon_2^{-1} + \varepsilon_3^{-1} + \varepsilon_4^{-1})^{-1}, & \Phi = H_z \end{cases} \quad (7.5)$$

Although Eqs. (7.3) and (7.4) can in principle treat the dielectric–dielectric and dielectric–metal interfaces, they will lose some accuracy at the interfaces and cannot well reproduce the features of exponentially decayed surface plasmon waves. Thus, a one-sided difference scheme is developed to rectify the problem. For the horizontal interface ( $y = y_h$ ) between the media 1 and 2, the flexible and high-order accurate one-sided difference reads

$$\left. \frac{\partial}{\partial y} \Phi^1 \right|_{x=i\Delta_x} \approx \frac{1.5\Phi^1(i,j) - 2\Phi^1(i,j-1) + 0.5\Phi^1(i,j-2)}{\Delta_y}$$

$$\left. \frac{\partial}{\partial y} \Phi^2 \right|_{x=i\Delta_x} \approx \frac{-1.5\Phi^2(i,j) + 2\Phi^2(i,j+1) - 0.5\Phi^2(i,j+2)}{\Delta_y} \quad (7.6)$$

For the vertical interfaces, one can also use the scheme.

The incident Sunlight reflected by OSC devices converts to outgoing waves propagating into infinite air (or free space) region. A perfectly matched layer (PML) [70] absorbs the outgoing waves without spurious reflections and “perfectly” simulates unbounded wave propagations. The wave equation with the complex coordinate stretched PML is given by [71]

$$\frac{1}{s_r(x)} \frac{\partial}{\partial x} \left( \frac{1}{s_r(x)} \frac{\partial \Phi}{\partial x} \right) + \frac{1}{s_r(y)} \frac{\partial}{\partial y} \left( \frac{1}{s_r(y)} \frac{\partial \Phi}{\partial y} \right) + k_0^2 \Phi = 0 \quad (7.7)$$

where  $s_r = 1 + i_0\sigma/\omega\epsilon_0$ ,  $i_0$  is the imaginary unit,  $\epsilon_0$  is the permittivity of free space, and the conductivities  $\sigma(x)$  and  $\sigma(y)$  are nonzeros only within PML layers normal to the  $x$ - and  $y$ -axes, respectively. The optimized conductivities are chosen as

$$\begin{aligned}\sigma_i &= \frac{0.02}{\Delta} \left( \frac{2i-1}{16} \right)^{3.7}, \quad i = 1, \dots, 8 \\ \sigma_{i+0.5} &= \frac{0.02}{\Delta} \left( \frac{2i}{16} \right)^{3.7}, \quad i = 0, \dots, 8\end{aligned}\quad (7.8)$$

where  $\Delta = \Delta_x$  or  $\Delta = \Delta_y$  for the PML layers normal to the  $x$ - or  $y$ -axis, and  $i$  is the grid index of the eight-layer PML.

At the outermost boundary of the PML, a Mur ABC [72] replacing the traditional perfectly electric conductor truncation boundary is employed to further reduce the spurious numerical reflections. Taking the top plane  $y = 0$  as an example, the second-order Mur ABC can be written as

$$\left[ \frac{\partial}{\partial y} + i_0 \left( k_0 + \frac{1}{2k_0} \frac{\partial^2}{\partial x^2} \right) \right] \Phi \Big|_{y=0} = 0 \quad (7.9)$$

and its discretized form is

$$f_1 \Phi(i, j) + f_2 \Phi(i-1, j) + f_3 \Phi(i+1, j) + f_4 \Phi(i, j+1) = 0 \quad (7.10)$$

where

$$\begin{aligned}f_1 &= 2 \exp(-i_0 k_0 \Delta_y) - 2k_0^2 \Delta_x^2 \exp(-i_0 k_0 \Delta_y) - 2 \\ f_2 &= f_3 = 1 - \exp(-i_0 k_0 \Delta_y) \\ f_4 &= 2k_0^2 \Delta_x^2\end{aligned}\quad (7.11)$$

Regarding a periodic OSC device, the periodic boundary conditions need to be implemented. According to the Floquet or Bloch theorem, we have

$$\begin{aligned}\Phi(x+P, y) &= \Phi(x, y) \exp(i_0 k_0 \sin \theta \cdot P) \\ \Phi(x, y) &= \Phi(x+P, y) \exp(-i_0 k_0 \sin \theta \cdot P)\end{aligned}\quad (7.12)$$

where  $P$  is the periodicity and  $\theta$  is the incident angle with respect to the  $y$ -axis.

It should be noted that the FDFD equations of (7.1) and (7.2) are specially for total field. The scattered field equations to be solved can be derived by using the relations

$$H_z = H_z^i + H_z^s \quad (7.13)$$

and

$$E_z = E_z^i + E_z^s \quad (7.14)$$



where  $E_z^i$  ( $H_z^i$ ) is the incident electric-field (magnetic-field), and  $E_z^s$  ( $H_z^s$ ) is the scattered electric-field (magnetic-field).

### 7.3.3 Volume Integral Equation Method

As a rigorous solution to Maxwell's equations, a volume integral equation (VIE) method [59] is developed to characterize the optical properties of 3D OSCs. Considering nonmagnetic optical materials with an arbitrary inhomogeneity profile, the VIE can be written as

$$\mathbf{E}^i(\mathbf{r}) = \frac{\mathbf{J}(\mathbf{r})}{-i_0\omega(\varepsilon(\mathbf{r}) - \varepsilon_0)} - i_0\omega\mu_0 \int_v \overline{\mathbf{G}}(\mathbf{r}, \mathbf{r}') \cdot \mathbf{J}(\mathbf{r}') d\mathbf{r}' \quad (7.15)$$

and

$$\mathbf{J} = -i_0\omega\mathbf{P} = -i_0\omega(\varepsilon - \varepsilon_0)\mathbf{E} \quad (7.16)$$

where  $i_0$  is the imaginary unit,  $\mathbf{E}^i(\mathbf{r})$  is the incident electric field of the light,  $\varepsilon(\mathbf{r})$  is the position-dependent permittivity of the inhomogeneous materials,  $\mathbf{J}$  is the volumetric polarization current to be solved, and  $\overline{\mathbf{G}}(\mathbf{r}, \mathbf{r}')$  is the dyadic Green's tensor in free space. The widely adopted approach for solving the VIE is the discrete dipole approximation (DDA) method [73]. Due to the hypersingularity of the Green's tensor and spurious discontinuity of the tangential  $E$ -field induced by the scalar (piecewise constant) basis functions, the DDA method cannot accurately characterize the subwavelength plasmonic physics [74] and breaks down in the multilayered device structure with high-contrast metallic nanostructures. Here, we develop an alternate algorithm to bypass the difficulties. In our model, the polarization currents are expanded using the roof-top vector basis functions [75], and thus the continuity of normal current is naturally satisfied at the material interfaces. Furthermore, the hypersingular Green's tensor is smoothed by using the finite-difference approximation.

From the VIE (7.15), the scattered electric field generated by the volumetric polarization current  $\mathbf{J}$  can be written as

$$\mathbf{E}^s(\mathbf{r}) = i_0\omega\mu_0 \int_v \overline{\mathbf{G}}(\mathbf{r}, \mathbf{r}') \cdot \mathbf{J}(\mathbf{r}') d\mathbf{r}' \quad (7.17)$$

Considering the Cartesian coordinate system, we use the short notation  $(u_1, u_2, u_3)$  instead of  $(x, y, z)$ , then we have

$$\begin{bmatrix} E_1^s \\ E_2^s \\ E_3^s \end{bmatrix} = \begin{bmatrix} L_{11} & L_{12} & L_{13} \\ L_{21} & L_{22} & L_{23} \\ L_{31} & L_{32} & L_{33} \end{bmatrix} \begin{bmatrix} J_1 \\ J_2 \\ J_3 \end{bmatrix} \quad (7.18)$$

where

$$L_{ij} = \begin{cases} L_{ii}^c + L_{ii}^q, & i = j \\ L_{ij}^q, & i \neq j \end{cases} \quad (7.19)$$

$$L_{ii}^c J_i = i_0 \omega \mu_0 \int_v g(\mathbf{r}, \mathbf{r}') J_i(\mathbf{r}') d\mathbf{r}' \quad (7.20)$$

$$L_{ij}^q J_j = \frac{i_0}{\omega \varepsilon_0} \frac{\partial}{\partial u_i} \int_v g(\mathbf{r}, \mathbf{r}') \frac{\partial J_j(\mathbf{r}')}{\partial u_j'} d\mathbf{r}' \quad (7.21)$$

where  $g(\mathbf{r}, \mathbf{r}')$  is the scalar Green's function, and  $\bar{\mathbf{G}}(\mathbf{r}, \mathbf{r}') = \left[ \bar{\mathbf{I}} + \frac{\nabla \nabla}{k_0^2} \right] g(\mathbf{r}, \mathbf{r}')$ .

Using the roof-top basis functions to expand the unknown currents, we have

$$\mathbf{J}(\mathbf{r}) = \sum_{i=1}^3 \mathbf{u}_i \sum_{k,m,n} J_i^D(k, m, n) T_{k,m,n}^i \quad (7.22)$$

where  $T_{k,m,n}^1$ ,  $T_{k,m,n}^2$ , and  $T_{k,m,n}^3$  are the volumetric roof-top functions given by

$$\begin{aligned} T_{k,m,n}^1 &= A_k(u_1) \Pi_m(u_2) \Pi_n(u_3) \\ T_{k,m,n}^2 &= \Pi_k(u_1) A_m(u_2) \Pi_n(u_3) \\ T_{k,m,n}^3 &= \Pi_k(u_1) \Pi_m(u_2) A_n(u_3) \end{aligned} \quad (7.23)$$

The functions  $A_k(u_1)$  and  $\Pi_m(u_2)$  are defined by

$$\begin{aligned} A_k(u_1) &= \begin{cases} 1 - \frac{|u_1 - k \Delta u_1|}{\Delta u_1}, & |u_1 - k \Delta u_1| \leq \Delta u_1 \\ 0, & \text{else} \end{cases} \\ \Pi_m(u_2) &= \begin{cases} 1, & |u_2 - (m - \frac{1}{2}) \Delta u_2| < \frac{\Delta u_2}{2} \\ 0, & \text{else} \end{cases} \end{aligned} \quad (7.24)$$

The cuboid cells are employed to discretize the structure to be modeled. Here,  $\Delta u_1$  and  $\Delta u_2$  are the grid sizes of each small cuboid along  $x$  and  $y$  directions, respectively. Other functions in (7.23) can be defined in the same way.

As a result, the discretized form for the operator  $L_{ii}^c$  in (7.20) can be written as

$$L_{ii}^{D,c} J_i^D = i_0 \omega \mu_0 g^D \otimes J_i^D \quad (7.25)$$

where  $\otimes$  denotes the discrete convolution

$$g^D \otimes J_i^D = \sum_{k',m',n'} g^D(k-k', m-m', n-n') J_i^D(k', m', n') \quad (7.26)$$

and

$$g^D(k, m, n) = \int_0^{\Delta u_1} \int_0^{\Delta u_2} \int_0^{\Delta u_3} g(u_{1,k} - u'_1, u_{2,m} - u'_2, u_{3,n} - u'_3) du'_1 du'_2 du'_3 \quad (7.27)$$

Likewise, the operator  $L_{12}^q$  in (7.21) can be discretized as

$$\begin{aligned} L_{12}^{D,q} J_2^D &= \frac{i_0}{\omega \varepsilon_0 \Delta u_1 \Delta u_2} [g^D(k+1, m, n) - g^D(k, m, n)] \\ &\quad \otimes [J_2^D(k, m, n) - J_2^D(k, m-1, n)] \\ &= \frac{i_0}{\omega \varepsilon_0 \Delta u_1 \Delta u_2} \{ [g^D(k+1, m, n) - g^D(k, m, n)] \\ &\quad - [g^D(k+1, m-1, n) - g^D(k, m-1, n)] \} \otimes J_2^D(k, m, n) \end{aligned} \quad (7.28)$$

where the finite-difference method is used for the smooth approximation of the dyadic Green's function.

The computations of the discrete convolutions can be performed efficiently by means of cyclic convolutions and FFT [76], which is similar to the DDA method. As a traditional iterative solver of the resulting VIE matrix equation, the conjugate-gradient method [77] converges very slowly and will produce the nonphysical random errors in the calculation of optical absorption. To tackle the problem, we employ the fast and smoothly converging biconjugate gradient stabilized (BI-CGSTAB) method [78] (See [Appendix](#)). The FFT is adopted to accelerate the matrix-vector multiplications encountered in the BI-CGSTAB solver with computational complexity of  $O(N \log N)$  and memory of  $O(N)$ .

### 7.3.4 Physical Quantities Extraction

Through the rigorous solutions to Maxwell's equations, we can access some important physical quantities to reveal the physical mechanism of plasmonic effects in OSCs and optimize device performances.

The absorption spectrum of OSCs is calculated by

$$S_A(\lambda) = \int_v n_r(\lambda) k_i(\lambda) \frac{2\pi c_0}{\lambda} \varepsilon_0 |\mathbf{E}|^2 dV \quad (7.29)$$

where  $n_c = n_r + i_0k_i$  is the complex refractive index of the active material,  $\lambda$  is the incident wavelength, and  $c_0$  is the speed of light in free space. It is worth mentioning that the absorption of metallic nanostructures should be precluded in the volume integral above. A spectral enhancement factor is the absorption spectrum of the OSC incorporating metallic nanostructures over that excluding the nanostructures.

Integrating with a standard solar irradiance spectrum (air mass 1.5 global), one can get the total absorption of OSCs

$$T_A = \int_{400 \text{ nm}}^{800 \text{ nm}} S_A(\lambda) \Gamma(\lambda) d\lambda \quad (7.30)$$

where  $\Gamma$  is the solar irradiance spectrum. Likewise, a total enhancement factor is the total absorption of the OSC incorporating metallic nanostructures over that excluding the nanostructures. In addition, a total absorptivity is also an important physical quantity to evaluate the absorption performance of OSCs, i.e.

$$A = \frac{\int_{400 \text{ nm}}^{800 \text{ nm}} S_A(\lambda) \Gamma(\lambda) d\lambda}{\int_{400 \text{ nm}}^{800 \text{ nm}} \Gamma(\lambda) d\lambda} \quad (7.31)$$

The exciton generation rate, which determines the short current of OSCs, can be written as

$$G(\mathbf{r}) = \int_{400 \text{ nm}}^{800 \text{ nm}} \frac{2\pi}{h} n_r(\lambda) k_i(\lambda) \epsilon_0 |\mathbf{E}(\mathbf{r})|^2 \Gamma(\lambda) d\lambda \quad (7.32)$$

where  $h$  is the Planck constant.

Except for the above physical quantities essential to the performance of OSC, there are several quantities that can facilitate understanding the physics of plasmonic effects. The scattering cross-section, which can estimate the scattering strength of a metallic nanostructure, is defined by [79, 80]

$$\sigma_s = \frac{\int_s \text{Re} \left[ \frac{1}{2} \mathbf{E}^s \times \text{conj}(\mathbf{H}^s) \right] \cdot d\mathbf{S}}{|\mathbf{S}_i|} \quad (7.33)$$

where “conj” denotes the complex conjugation,  $S$  is an arbitrary surface enclosing the metallic nanostructure,  $\mathbf{S}_i = \frac{1}{2} [\mathbf{E}^i \times \text{conj}(\mathbf{H}^i)]$  is the incident energy flux, and  $\mathbf{E}^s$  and  $\mathbf{H}^s$  are the scattered electric and magnetic fields, respectively. Considering the total power absorbed by a metallic nanostructure, the absorption cross-section is of the form [79, 80]

$$\sigma_a = - \frac{\int_v \text{Re} \left[ \frac{1}{2} \mathbf{E} \times \text{conj}(\mathbf{H}) \right] \cdot d\mathbf{S}}{|\mathbf{S}_i|} = \frac{\int_v k_0 \epsilon_r''(\mathbf{r}) |\mathbf{E}(\mathbf{r})|^2 dV}{|\mathbf{E}^i|^2} \quad (7.34)$$

where  $\epsilon_r''$  is the imaginary part of relative permittivity. The extinction (total) cross-section describes the intrinsic losses of a plasmonic system including both absorption loss and scattering (or leaky) loss. Hence, the sum of the scattering and the absorption cross-section is the extinction cross-section. Moreover, we have another mathematical expression for the extinction cross-section by making use of the optical theorem at the far-field limit [80]

$$\sigma_e = \frac{4\pi}{k_0} \text{Im}[\mathbf{e}^i \cdot \bar{\mathbf{F}} \cdot \mathbf{e}^i] \quad (7.35)$$

and

$$\mathbf{E}^s = \frac{\exp(i_0 k_0 r)}{r} \bar{\mathbf{F}} \cdot \mathbf{E}^i, \quad r \rightarrow \infty \quad (7.36)$$

where  $\mathbf{e}_i$  is the polarization unit vector of the incident electric field  $\mathbf{E}^i$ .

To understand the mode hybridization for plasmon coupling, the polarization charge distribution on the surface of metallic nanostructure is given as follows

$$\rho_p = \nabla \cdot (\epsilon_0 \mathbf{E}) = -\nabla \cdot \mathbf{P} \quad (7.37)$$

where  $\mathbf{P} = (\epsilon - \epsilon_0)\mathbf{E}$  is the polarization density. Based on the divergence-free condition, the polarization charge is definitely zero except on the heterogeneous boundaries.

The Fabry-Pérot mode or quasi-guided mode can be characterized by analyzing the averaged power density of electromagnetic waves flowing within an active or a grating layer along the lateral direction of OSC devices, which is expressed in

$$P_x = \frac{1}{2} \text{Re}[E_y H_z^\dagger - E_z H_y^\dagger] \quad (7.38)$$

where “ $\dagger$ ” is a notation of complex conjugation and the power density flows along the  $x$  direction.

## 7.4 Results and Discussions

We will review plasmonic effects of typical metallic nanostructures by involving their functionalities and performances in manipulating the optical properties of OSCs. The SPR, LPR, and their hybridization are investigated in the three following cases [16, 30, 33]. In modeling OSCs, the complex refractive indices of metals (Au, Ag, etc) and organic materials can be expressed by the Brendel-Bormann model [81] and measured from ellipsometry [82, 83], respectively. It is worth mentioning that standard solar irradiance spectrum (air mass 1.5 global) is taken into account in our theoretical models.

### 7.4.1 Periodic Back Nanostrrips

We systematically study the angular response of a thin-film OSC with a periodic metal back nanostrrips. The generalized equation of Lambert's cosine law for arbitrary periodic structure is formulated. We find that the periodic strip structure can achieve wide-angle absorption enhancement compared with the (planar) nonstrip structure for both the TE- and TM-polarized light. The quasi-guided modes supported by the periodic strip structure contribute to the enhancement for the TE-polarized light. The SPRs excited by the subwavelength Au nanostrrips contribute to the enhancement for the TM-polarized light.

The energy conservation law in a periodic structure is given by

$$[1 - L(\theta)] \cdot \int \frac{-1}{2} \text{Re}[\mathbf{E}^i \times \text{conj}(\mathbf{H}^i)] \cdot d\mathbf{S} = \int n_r k_i \omega \varepsilon_0 |\mathbf{E}|^2 dV \quad (7.39)$$

where  $\mathbf{E}^i$  and  $\mathbf{H}^i$  are the incident electric and magnetic fields,  $\mathbf{S}$  is a virtual planar surface in front of a unit cell of the SC,  $n_c = n_r + i_0 k_i$  are the complex refractive indices of the active materials, and  $L(\theta)$  is an energy loss fraction. One part of the energy loss is the scattering loss, which can be characterized by the summation of the reflectance and transmittance of the periodic structure [66]. The scattering loss can be reduced by the light guiding, enhancement, and trapping schemes. Another part of the energy loss is the metallic absorption loss, which can be reduced by engineering the metal's size, material, and position. The irradiance of the Sun is the incident power per unit area of an electromagnetic radiation at the surface, i.e.

$$I = \frac{-1}{2} \text{Re}[\mathbf{E}^i \times \text{conj}(\mathbf{H}^i)] \cdot \mathbf{n} = \frac{|\mathbf{E}^i|^2}{2Z_0} \cos \theta \quad (7.40)$$

where  $Z_0 = \sqrt{\mu_0/\varepsilon_0}$  is the wave impedance of free space and  $\theta$  is the incident angle of the sunlight with respect to the normal direction of the surface  $\mathbf{S}$ . For the Lambertian bulk cells, which have an angle-independent energy loss fraction  $L$ , the absorption of the active layers represented by the right hand of Eq. (7.39) obeys Lambert's cosine law that the absorption is a cosine function of the incident angle  $\theta$ . Eq. (7.39) is a generalized equation of Lambert's cosine law for any periodically structured SCs.

Figure 7.2a illustrates a typical structure of standard OSCs without any optimizations. The heterojunction active layer is composed of copper phthalocyanine (CuPc) and fullerene ( $C_{60}$ ) as an electron donor and acceptor, respectively. The bathocuproine (BCP) layer is a spacer layer for extracting electrons. A metallic back nanopattern is made from an Au strips and Poly(3,4-ethylenedioxythiophene):poly(4-styrenesulfonic acid) (PEDOT:PSS; AI4083) that can collect holes. We use the FDFD method presented in Sect. 7.3.2 to calculate the angular response of the OSC. For the angular response simulation, a challenging problem lies at the wide angle ( $0^\circ$ – $90^\circ$ ) and broadband (400–800 nm) calculations. We employ the high-performance parallel computing technique to tackle the problem.

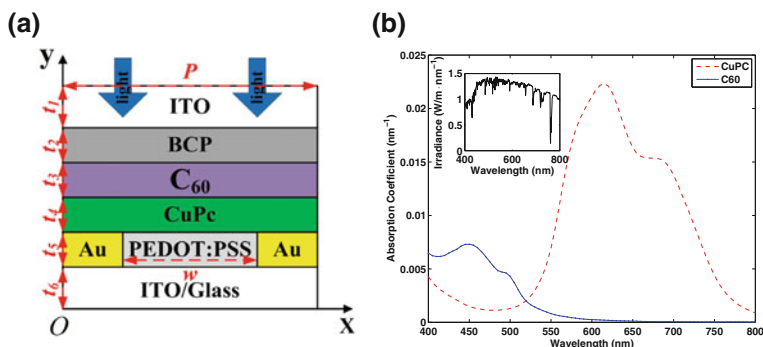


**Fig. 7.2** **a** The schematic structure of a unit cell of the flat-heterojunction OSC. The structural parameters are  $t_1 = 100$  nm,  $t_2 = 10$  nm,  $t_3 = 40$  nm,  $t_4 = 30$  nm,  $t_5 = 30$  nm,  $t_6 = 100$  nm,  $w = 100$  nm, and  $P = 200$  nm; **b** the absorption coefficients of CuPc and C<sub>60</sub>. The *inset* is the solar irradiance spectrum of an air mass 1.5 global. ©2011 OSA; Ref. [16]

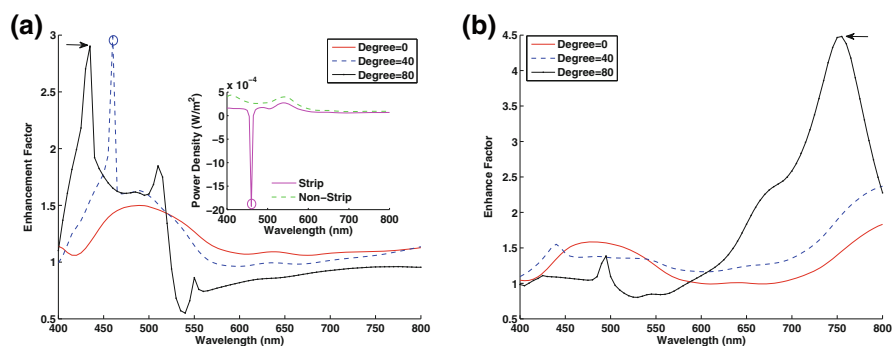


**Fig. 7.3** The absorption of the periodic strip structure is compared to that of the nonstrip structure replacing the laterally periodic Au-PEDOT:PSS-Au pattern by the planar PEDOT:PSS layer. The near-field profiles of the absorption peaks pointed by the *arrows* are shown in Fig. 7.4. **a** The absorption enhancement factor for the TE polarization. The *inset* shows the averaged power density of the Au-PEDOT:PSS-Au pattern along the  $x$  direction calculated by Eq. (7.38). The negative power density peak due to the opposite propagation direction coincides with the absorption peak at  $\theta = 40^\circ$  with the wavelength of 460 nm; **b** the absorption enhancement factor for the TM polarization. ©2011 OSA; Ref. [16]

Figure 7.2b shows the absorption coefficients of CuPc and C<sub>60</sub>. The separated absorption peaks can improve the light absorption of OSCs, which can be realized by different enhancement mechanisms with respect to different materials. Compared with the absorption of the nonstrip structure making from the planar PEDOT:PSS layer, the enhancement factors of the absorption for the strip structure of the laterally periodic Au-PEDOT:PSS-Au pattern are shown in Fig. 7.3a, b for the TE and TM polarizations, respectively.

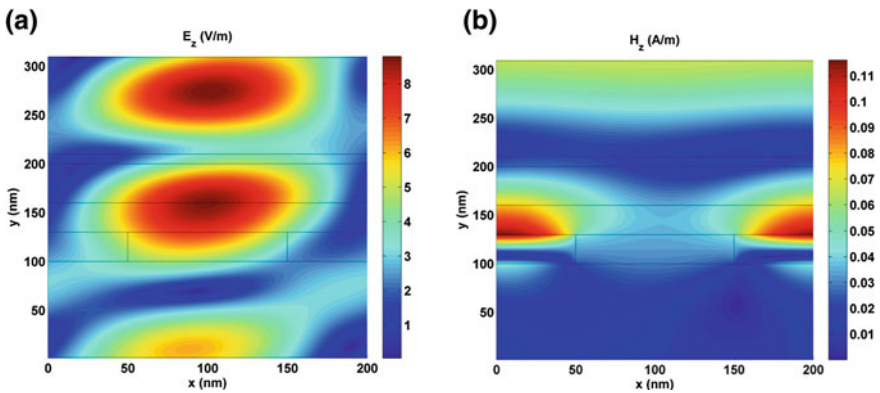
For the TE polarization, the absorption enhancement is obtained from 400 to 500 nm with the very strong absorption peaks, especially at the oblique angles.

The rapid and extraordinary variations in the absorption over narrow frequency bands imply the resonant Wood's anomalies with asymmetric Fano line shape [36, 37]. Figure 7.4a shows the  $E$ -field of the absorption peak pointed by the arrow in Fig. 7.3a for the Wood's anomalies. The intense  $E$ -field in the active layer is bounded between the periodic nanostrip pattern and the BCP layer. The  $E$ -field is related to the quasi-guided modes supported by the periodic strip structure with the phase-matching condition of  $k_0 \sin \theta + 2\pi m/P = \pm \text{Re}(\beta)$ ,  $m = 0, \pm 1, \pm 2, \dots$ , where  $P$  is the periodicity,  $k_0$  is the incident wave number, and  $\beta$  is the complex propagation constant of the quasi-guided modes. The condition is easily satisfied in standard OSCs in view of the broadband and wide angle Sun illumination. For confirming the forced-resonance behavior of the Wood's anomalies, we calculate the averaged power density flowing in the  $x$  direction for the Au-PEDOT:PSS-Au pattern (strip structure) and PEDOT:PSS layer (nonstrip structure). For the strip structure, as shown in the inset of Fig. 7.3a, the negative (opposite direction) power density peak induced by the  $n = -1$  space harmonics coincides with the absorption peak at  $\theta = 40^\circ$  and 460 nm. In addition, the spectral overlap between the Wood's anomalies and the material absorption of  $C_{60}$  will be of a good help for short wavelength photon harvesting. Particularly, we can observe the sharp oscillations of the enhancement factor at  $\theta = 80^\circ$  from 510 to 550 nm. The sharp oscillations result from the overlap between the Fabry-Pérot mode in the nonstrip structure and the quasi-guided mode in the strip structure. It should be noted that the quasi-guided mode is an eigenmode of Maxwell's equations for arbitrary periodic structure and cannot be excited in the planar nonstrip structure by the plane wave due to the momentum mismatch ( $\beta > k_0$ ). However, the Fabry-Pérot mode can be found in the planar structure, and can be understood by the mode coupling between the excitation solution and the eigenmode.

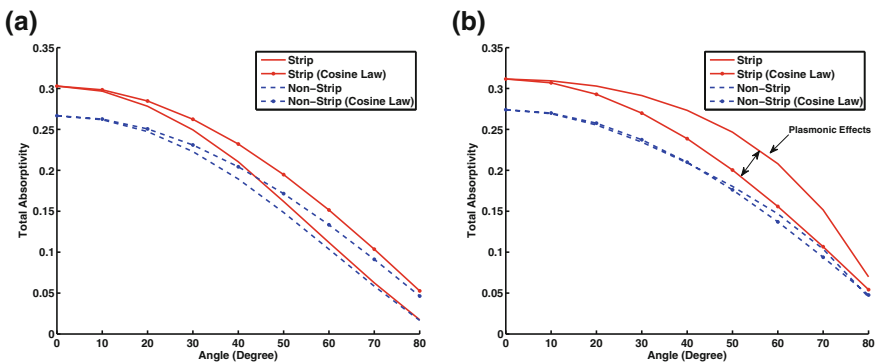
For the TM polarization, a broadband absorption enhancement is obtained from 650 to 800 nm, especially at the oblique angles. Figure 7.4b shows the  $H$ -field of the absorption peak pointed by the arrow in Fig. 7.3b. The concentrated  $H$ -field at the interface between Au and CuPc layers is due to the SPRs excited by the evanescent waves produced by the subwavelength nanostrips. Regarding the absorption peaks around 750–800 nm in Fig. 7.3b, they are blue shifted as the incident angle increases due to the blue shift of the plasmon-coupled Fabry-Pérot mode. By studying the SPR spectrum (Fig. 7.3b; black straight-dotted line) and the absorption spectrum of CuPc (Fig. 7.2b; red dashed line) together, it is observed that the SPR peak at 675 nm is weaker than that at 755 nm because of the stronger absorption of CuPc at 675 nm.

Figure 7.5a, b shows the total absorptivity defined in Eq. (7.31) as a function of the incident angle, respectively, for the TE and TM polarizations. The ideal total absorptivity governed by the generalized Lambert's cosine law is calculated by  $A_0 \cos \theta$ , where  $A_0$  is the total absorptivity under the vertical incidence condition. The total absorptivity of the strip structure is noticeably better than that of the nonstrip structure for both polarizations. The improvements are caused by the Wood's anomalies and the SPRs that have been explained previously. When the incident angle increases, the total absorptivity for the TM polarization decays





**Fig. 7.4** **a**  $E_z$  field profile of the TE polarization at  $\theta = 80^\circ$  with the wavelength of 435 nm; **b**  $H_z$  field profile of the TM polarization at  $\theta = 80^\circ$  with the wavelength of 755 nm. ©2011 OSA; Ref. [16]



**Fig. 7.5** The total absorptivity as a function of the incident angle  $\theta$ . The generalized Lambert’s cosine law (*straight-dotted* and *dash-dotted curves*) is calculated by  $A_0 \cos \theta$ , where  $A_0$  is the total absorptivity under the vertical incidence condition. **a** TE polarization; **b** TM polarization. ©2011 OSA; Ref. [16]

slower than that for the TE polarization, which is independent of the structure. This feature may be understood by the fact that better light confinement can be achieved for the TM-polarized light where the  $E$ -field is not continuous across inhomogeneous material interfaces. For the TE polarization, the absorption of the strip structure becomes comparable to that of the nonstrip structure near grazing angles. The narrow absorption peaks due to the Wood’s anomalies can improve the total absorption, but the improvement is smaller than that from the SPRs in the TM-polarized light. For the TM polarization, the plasmon-induced absorption enhancement strongly breaks the limit of the generalized Lambert’s cosine law and shows the “super-Lambertian” absorption. The broadband and wide-angle

absorption enhancements by the SPRs will be of a great help for high-efficiency photovoltaic cells.

In conclusion, we have formulated the equation of the generalized Lambert's cosine law and comprehensively studied the Au nanostrip OSC structure for enhancing the TE- and TM-polarized light with the detailed explanations of the enhancements by the Wood's anomalies and SPRs.

### 7.4.2 Multiple Nanospheres

We studied in detail on the near-field multiple scattering effects of plasmonic nanospheres (NSPs) embedded into thin-film OSCs. The fundamental physics of the optical absorption shows remarkable differences between the NSPs embedded into a spacer and those embedded into an active layer. The direction-dependent features of near-field scattering from NSPs significantly affect the absorption enhancement when NSPs are embedded into the spacer. The interaction between longitudinal and transverse modes supported in the NSP chain plays a key role in the absorption enhancement when NSPs are embedded into the active layer. Through properly engineering the position and spacing of NSPs, our theoretical results show that the absorption enhancement can be improved by about 100%. Moreover, we demonstrate the breakdown of the electrostatic scaling law that should be considered in the design of OSCs. The work provides the physical guidelines for plasmonic OSCs.

Figure 7.6a, b illustrates a schematic pattern of a bulk heterojunction OSC nanostructure [2, 3] to be investigated. The active layer is a typical blend polymer of P3HT (poly(3-hexylthiophene)) and PCBM (methanofullerene). A hole conduction layer is PEDOT:PSS chosen as a spacer between an electrode and the active layer. Figure 7.6c shows the absorption coefficient of the active material. With tunable size and spacing, a spherical chain comprising multiple silver (Ag) NSPs is embedded into the spacer or active layer as near-field concentrators. An incident light is propagated from the spacer to the active layer with a TM polarization ( $H_z^i = 0$ ) at a vertical ( $0^\circ$ ) and an oblique ( $60^\circ$ ) incidences. In comparison with the TE polarization, the TM polarization supports much stronger dipole-dipole couplings between NSPs. Moreover, the absorption enhancement by a silver NSP array, which has a polarization-independent feature, can be regarded as a superposition of those by silver NSP chains with both the TM and TE polarizations. To unveil device-related multiple scattering mechanism of NSPs, we develop a rigorous VIE method presented in Sect. 7.3.3 to characterize the optical properties of the OSC. The coupling between multiple NSPs, as well as the interaction between NSPs and multilayer device structure, is fully taken into account in our model. It is worth mentioning that we only calculate the optical absorption of the active material excluding the metallic absorption of NSPs especially when NSPs are embedded into the active layer. Figures 7.7 and 7.8 show the spectral enhancement factors (defined

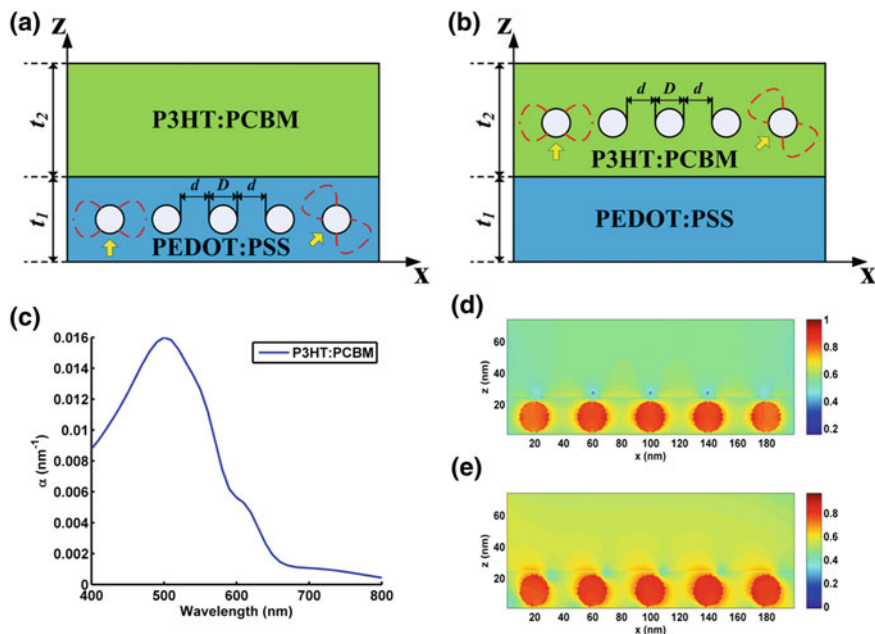


**Fig. 7.6** **a, b** A schematic OSC nanostructure. To enhance the optical absorption of the OSC, a spherical chain comprising multiple NSPs is embedded into a spacer layer (PEDOT:PSS) or into an active layer (P3HT:PCBM). The geometric size is  $t_1 = 1.25D$  and  $t_2 = 2.5D$ . The spacing between adjacent NSPs is  $d = D$  or  $d = 0.2D$  for the separated or close-packed ones, respectively. The diameter is  $D = 20$  or  $D = 40$  nm for the small or large NSPs, respectively. The *yellow arrows* represent the propagation direction of an incident light with a TM polarization ( $H_z^i = 0$ ) and the *red dashed lines* denote corresponding near-field profiles of NSPs. **c** Absorption coefficient of the active material. **d, e** Near-field polarization current distributions of the OSC nanostructure at a vertical and an oblique incidences, respectively. ©2011 AIP; Ref. [30]

in Sect. 7.3.4). Table 7.1 lists the total enhancement factors (defined in Sect. 7.3.4) corresponding to Figs. 7.7 and 7.8.

When Ag NSPs are embedded into the spacer, as the incident angle increases, both the spectral and total enhancement factors increase independent of the NSP's size and spacing. The fundamental physics is that the near-field energy of a metal nanoparticle is mainly distributed along the polarization direction of incident  $E$ -field, which is critically different from the far-field scattering, where the energy scatters to the propagation direction of the incident light. As shown in Fig. 7.6a, d, the concentrated electric near field is distributed along the lateral direction at the vertical incidence, which deters the plasmonic resonance from enhancing the light absorption of the active material even though very strong near field is obtained. Hence, a careful design in introducing NSPs into a multilayer device structure is critical for enhancing the performances of plasmonic OSCs. Interestingly, absorption enhancement improves at the oblique incidence, because more energy transfers to the active layer having a significant directivity as depicted in Fig. 7.6e.

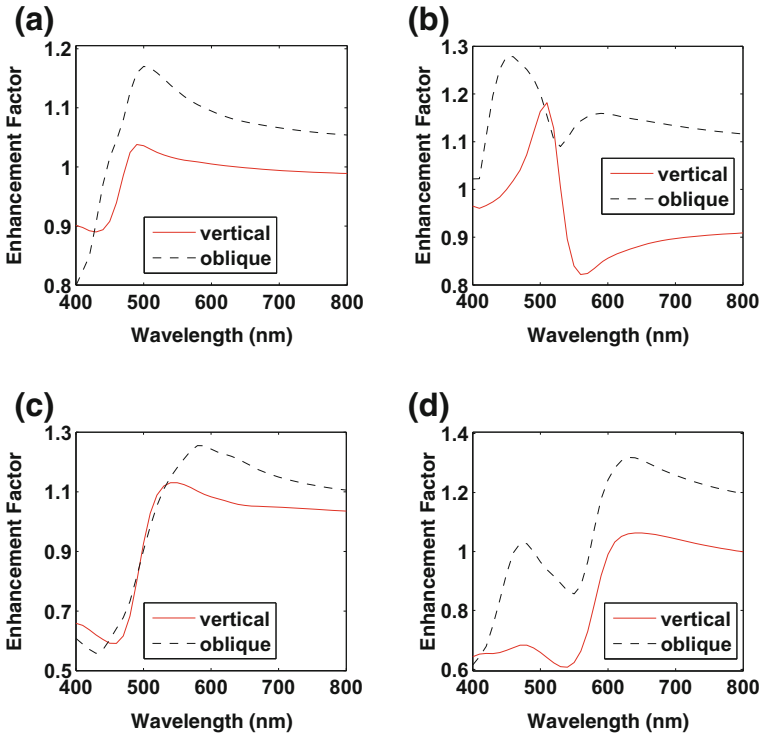


**Fig. 7.7** The spectral enhancement factors of the OSC with NSPs are embedded into the spacer. The angular responses of the OSC for the vertical ( $0^\circ$ ) and oblique ( $60^\circ$ ) incidences are also shown: **a** separated small NSPs; **b** close-packed small NSPs; **c** separated large NSPs; **d** close-packed large NSPs. ©2011 AIP; Ref. [30]

It should be noticed that since the thickness of the active layer is thinner than one half of wavelength, near-field (not far field) physics plays a key role in the optical design of NSPs incorporated OSCs. Compared to the spectral enhancement factors for the separated NSPs, a deep dip can be observed for the close-packed ones as shown in Fig. 7.7b, d. The dips resulting from the metallic absorption of the NSPs correlate with the coupling resonance of the NSP chain. The close-packed NSPs, particularly for the large ones, block the light and absorb a large amount of sunlight energy. As a result, little energy penetrates into the active material. Due to the  $R^{-3}$  decay of electric near-field and the reflection by the interface between the spacer and active layer, the absorption enhancement is very small when NSPs are embedded into the spacer. Comparing Fig. 7.7d to Fig. 7.7b, the large close-packed NSPs with large scattering cross-section have more significant enhancement away from resonance but induce deeper dips near the resonance. Weighting the two effects, the large close-packed NSPs have smaller total enhancement factor as listed in Table 7.1.

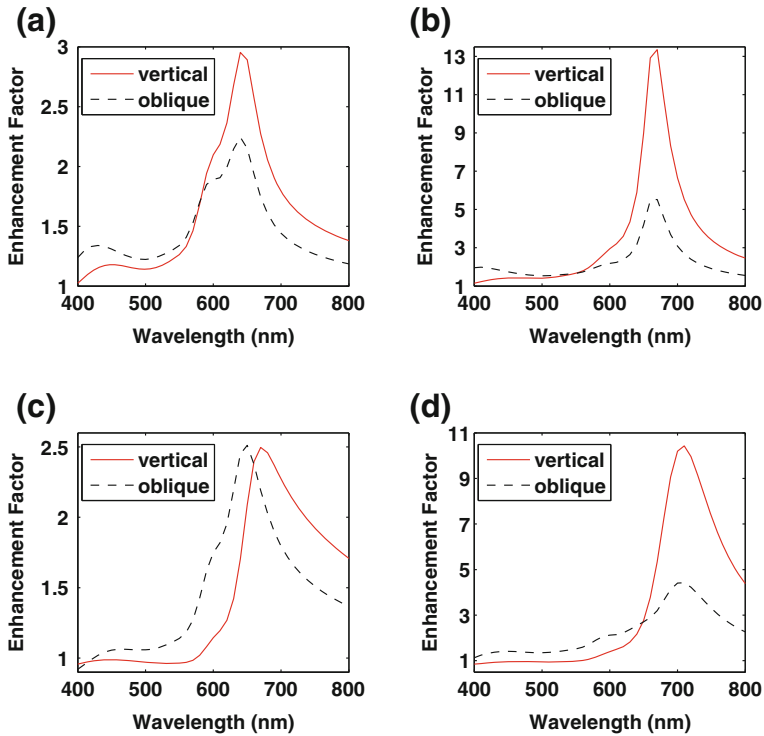


**Fig. 7.8** The spectral enhancement factors of the OSC with NSPs are embedded into the active layer. The angular responses of the OSC for the vertical ( $0^\circ$ ) and oblique ( $60^\circ$ ) incidences are also shown: **a** separated small NSPs; **b** close-packed small NSPs; **c** separated large NSPs; **d** close-packed large NSPs. ©2011 AIP; Ref. [30]

**Table 7.1** Total enhancement factors for the NSPs embedded into the spacer and active layer. ©2011 AIP; Ref. [30]

Spacer layer	Vertical incidence	Oblique incidence
Separated small	0.992	1.078
Close-packed small	0.989	1.174
Separated large	0.927	0.935
Close-packed large	0.725	0.960
Active layer	Vertical incidence	Oblique incidence
Separated small	1.366	1.374
Close-packed small	1.985	1.821
Separated large	1.118	1.216
Close-packed large	1.342	1.589

In contrast to the NSPs embedded into the spacer, our results show that the NSPs embedded into the active layer offer stronger optical absorption, which can be observed in Table 7.1. As seen in Fig. 7.6b, the scattering energy from the NSPs is directly and sufficiently absorbed by the contiguous active material uncorrelated with the directional property of the electric near field. Owing to the plasmon coupling and hybridization, the close-packed NSPs have more concentrated near-field distribution leading to larger enhancement (Table 7.1). Remarkably, the absorption of the OSC has about 2-fold increase by the small close-packed NSPs. For the large close-packed NSPs, the excessive red-shifted resonance reduces the spectral overlap between the resonance and the absorption peak of the active material as illustrated in Figs. 7.8d and 7.6c. At vertical incidence, the reduced spectral overlap gives a reason why the total enhancement factor by the large close-packed NSPs is smaller than that by the small ones. However, the total enhancement factor by the large close-packed NSPs increases at oblique incidence, which distinguishes from the close-packed small NSPs. The interplay between longitudinal and transverse modes [40, 84] supported by the NSP chain is a physical origin of the phenomenon. Having larger geometric size and stronger retardation effect, the large close-packed NSPs support more red-shifted longitudinal modes at the vertical incidence and more blue-shifted transverse modes at the oblique incidence (see Fig. 7.8b, d). In comparison with the red-shifted longitudinal modes, the blue-shifted transverse modes have a better spectral overlap with the absorption coefficient of the active material and can be further exploited or engineered in a future design of OSCs.

Regarding the electrostatic limit described by the Laplace equation, the near-field or far-field response of a subwavelength scatterer is independent of the scatterer's size and depends only on its shape [85]. Therefore, it may cause a misunderstanding that the same enhancement can be obtained if the scaling ratio of a device structure to a concentrator remains constant. However, using the same scaling ratio as shown in Fig. 7.6a, b, we find that the large NSPs and small ones have noticeable differences both in the spectral and total enhancement factors. The breakdown of the scaling law can be explained by the retarded and multiscale effects. The electromagnetic response of a single NSP is dominated by the electrostatic (nanocircuit) physics, but that of multiple NSPs is governed by the electrodynamic (wave) physics with nonnegligible retardation and long-range interplay between each NSPs. Furthermore, large-scale OSC nanostructure and small-scale NSPs strongly couple with each other, which makes the optical path very complicated; and the trapping confinement, together with leaky loss, must be considered quantitatively.

In conclusion, we study the near-field multiple scattering effects of plasmonic NSPs embedded into the thin-film OSC. The absorption enhancement of the OSC strongly depends on the directional property of near-field scattering from NSPs and the interplay between longitudinal and transverse modes supported for the NSPs embedded into the spacer and active layer, respectively. Moreover, the complex coupling between NSPs and device makes the scaling law in electrostatics inapplicable. The work provides the fundamental physical understanding and design guidelines for a typical class of plasmonic photovoltaics.

### 7.4.3 Hybrid Plasmonic System

We propose a novel optical design of OSC with a hybrid plasmonic system, which comprises a plasmonic cavity coupled with a dielectric core-metal shell (DC-MS) nanosphere. It has been investigated that optical absorption of the active polymer material has a 4-fold increase. With the help of rigorous VIE method presented in Sect. 7.3.3, we unveil the fundamental physics of the significant enhancement, which mainly attributes to the coupling of symmetric surface wave modes supported by the cavity resonator. We further demonstrate that the optical enhancement strongly depends on the decay length of surface plasmon waves penetrated into the active layer. Moreover, coherent interaction between the cavity and the DC-MS nanosphere is definitely confirmed by our theoretical model. A distribution of polarization charges on the surface of the cavity indicates a bonding and antibonding coupling modes [42] in the hybrid plasmonic system. The work introduces a new hybrid plasmonic cavity device structure to enhance the optical absorption of organic photovoltaics with detailed physical explanations.

Figure 7.9 shows the schematic pattern of a heterojunction OSC. A hybrid plasmonic system, which comprises a plasmonic cavity coupled with a dielectric core-metal shell nanosphere, is employed for improving the optical absorption of the active polymer material. A transparent spacer is inserted to avoid local shunt and extract carriers. The incident light is propagated from the spacer to the active layer at the vertical incident angle with an  $E$ -field polarized along the  $x$  direction. Figure 7.10a shows the real and imaginary parts of the refractive index of the active material.

First, various nanosphere concentrators (excluding the plasmonic cavity) are systematically and comparatively observed. These nanospheres include a dielectric sphere, a metal sphere, a metal core-dielectric shell (MC-DS) sphere, and a dielectric core-metal shell (DC-MS) sphere. The scattering cross-section (SCS) of the nanospheres can be obtained from the generalized reflection coefficients of the spherically layered media [59, 79, 80]

$$\sigma_s = \frac{2\pi}{K_3^2} \sum_{m=1}^{\infty} (2m+1) \left( \left| \tilde{R}_{3,2}^{\text{TM}}(m) \right|^2 + \left| \tilde{R}_{3,2}^{\text{TE}}(m) \right|^2 \right) \quad (7.41)$$

where 1, 2, and 3 denote the core, shell, and active layers as shown in Fig. 7.9, respectively,  $m$  is the order of the modified spherical Bessel (Hankel) functions, and  $\tilde{R}_{3,2}^{\text{TM}}$  and  $\tilde{R}_{3,2}^{\text{TE}}$  are the generalized reflection coefficients of the TM and TE spherical waves in the layer 3 reflected by the layer 2. For small spherical particles, the leading term ( $m = 1$ ) of  $\tilde{R}_{3,2}^{\text{TM}}$  determines the value of the SCS. The generalized reflection coefficient can be written as a recursive equation

$$\tilde{R}_{i,i-1}^{\text{TM}} = R_{i,i-1}^{\text{TM}} + \frac{T_{i-1,i}^{\text{TM}} \tilde{R}_{i-1,i-2}^{\text{TM}} T_{i,i-1}^{\text{TM}}}{1 - R_{i-1,i}^{\text{TM}} \tilde{R}_{i-1,i-2}^{\text{TM}}} \quad (7.42)$$

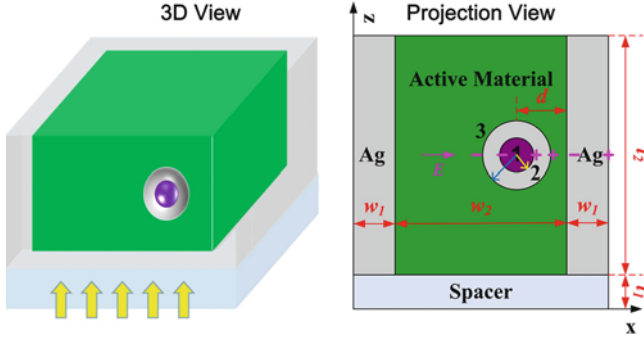


**Fig. 7.9** The schematic pattern of a heterojunction OSC. A hybrid plasmonic system, which comprises a plasmonic cavity coupled with a dielectric core-metal shell nanosphere, is employed for improving the optical absorption of the active polymer material. A transparent spacer is inserted to avoid local shunt and extract carriers. The structural parameters are  $t_1 = 20$  nm,  $t_2 = 60$  nm,  $w_1 = 30$  nm,  $w_2 = 90$  nm, and  $d = 21$  nm. The radius of the core layer (denoted by the *yellow arrow*) and that of the shell layer (denoted by the *blue arrow*) are set to  $r_1 = 7.5$  nm and  $r_2 = 15$  nm, respectively. For a bonding coupling mode in the hybrid system, the polarity of its polarization charge is also marked. ©2011 OSA; Ref. [33]

and

$$R_{i,i+1}^{\text{TM}} = \frac{\sqrt{\varepsilon_{i+1}\mu_i}\hat{H}_m^{(1)}(K_{i+1}r_i)\hat{H}_m^{(1)'}(K_i r_i) - \sqrt{\varepsilon_i\mu_{i+1}}\hat{H}_m^{(1)}(K_{i+1}r_i)\hat{H}_m^{(1)}(K_i r_i)}{\sqrt{\varepsilon_i\mu_{i+1}}\hat{J}_m(K_i r_i)\hat{H}_m^{(1)'}(K_{i+1}r_i) - \sqrt{\varepsilon_{i+1}\mu_i}\hat{H}_m^{(1)}(K_{i+1}r_i)\hat{J}_m'(K_i r_i)} \quad (7.43)$$

$$T_{i,i+1}^{\text{TM}} = \frac{i_0\varepsilon_{i+1}\sqrt{\mu_{i+1}/\varepsilon_i}}{\sqrt{\varepsilon_i\mu_{i+1}}\hat{J}_m(K_i r_i)\hat{H}_m^{(1)'}(K_{i+1}r_i) - \sqrt{\varepsilon_{i+1}\mu_i}\hat{H}_m^{(1)}(K_{i+1}r_i)\hat{J}_m'(K_i r_i)} \quad (7.44)$$

$$R_{i,i-1}^{\text{TM}} = \frac{\sqrt{\varepsilon_i\mu_{i-1}}\hat{J}_m(K_i r_{i-1})\hat{J}_m'(K_{i-1}r_{i-1}) - \sqrt{\varepsilon_{i-1}\mu_i}\hat{J}_m'(K_i r_{i-1})\hat{J}_m(K_{i-1}r_{i-1})}{\sqrt{\varepsilon_{i-1}\mu_i}\hat{J}_m(K_{i-1}r_{i-1})\hat{H}_m^{(1)'}(K_i r_{i-1}) - \sqrt{\varepsilon_i\mu_{i-1}}\hat{H}_m^{(1)}(K_i r_{i-1})\hat{J}_m'(K_{i-1}r_{i-1})} \quad (7.45)$$

$$T_{i,i-1}^{\text{TM}} = \frac{i_0\varepsilon_{i-1}\sqrt{\mu_{i-1}/\varepsilon_i}}{\sqrt{\varepsilon_{i-1}\mu_i}\hat{J}_m(K_{i-1}r_{i-1})\hat{H}_m^{(1)'}(K_i r_{i-1}) - \sqrt{\varepsilon_i\mu_{i-1}}\hat{H}_m^{(1)}(K_i r_{i-1})\hat{J}_m'(K_{i-1}r_{i-1})} \quad (7.46)$$

where  $r_i$ ,  $\varepsilon_i$ ,  $\mu_i$ , and  $K_i$  are the radius, permittivity, permeability, and wave number of the  $i$ th spherical layer, respectively. Figure 7.10b, c shows the spectral enhancement factors (defined in Sect. 7.3.4) and the SCS of the nanospheres,



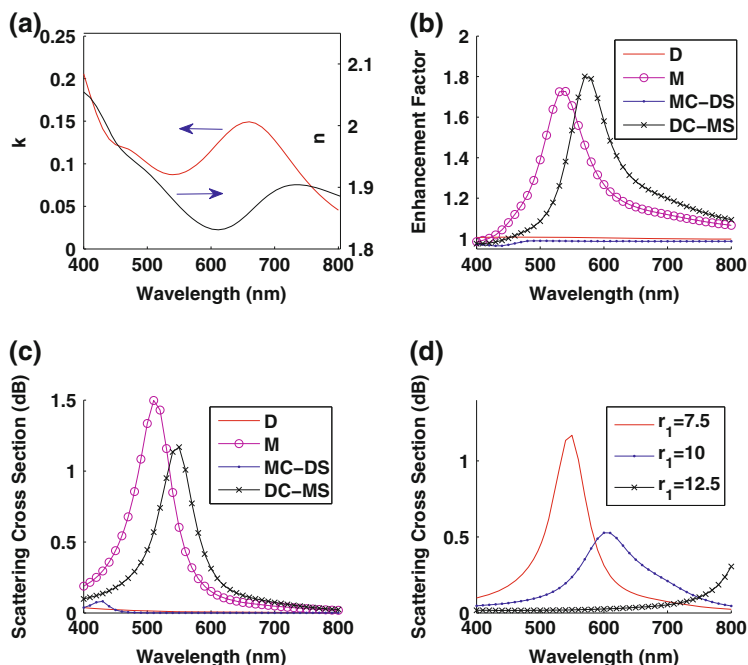


**Fig. 7.10** **a** The real and imaginary parts of the refractive index of the active material; **b** the spectral enhancement factors for various nanospheres. D denotes the dielectric sphere ( $n = 4$ ,  $k = 0$ ), M denotes the metal silver sphere, MC-DS denotes the metal core-dielectric shell sphere, and DC-MS denotes the dielectric core-metal shell sphere. The  $\text{SiO}_2$  and Ag as a dielectric and metal layers are adopted for the core-shell spheres; **c** the scattering cross-section (SCS) of the nanospheres; **d** the SCS of the DC-MS sphere as a function of the core radius (nm). ©2011 OSA; Ref. [33]

respectively. As seen in Fig. 7.10b, c, the peaks of the enhancement factors agree with those of the SCS well. The small dielectric nanosphere, although has no loss and large refractive index ( $n = 4$ ), is not a good concentrator for OSCs. The dielectric nanosphere with positive refractive index cannot produce strong dipole resonance compared to the metal nanosphere. Moreover, in contrast to the DC-MS sphere that has a metal layer adjacent to different materials ( $\text{SiO}_2$  and polymer), the resonance of the MC-DS sphere is blue-shifted, because only one material  $\text{SiO}_2$  with lower refractive index is adjacent to the metal layer. The near field of the MC-DS sphere confines to the shell layer and cannot sufficiently scatter to the active layer. As a result, the optical enhancement by the MC-DS sphere is very weak. Figure 7.10d shows a tunable plasmon resonance by engineering the geometry of the DC-MS sphere. The resonance is red shifted and becomes damped as the core radius increases.

Second, we investigate the plasmonic silver cavity structure enclosing the active polymer material. Here the nanosphere is excluded. Figure 7.11a shows the spectral enhancement factor by the plasmonic cavity. A broadband enhancement

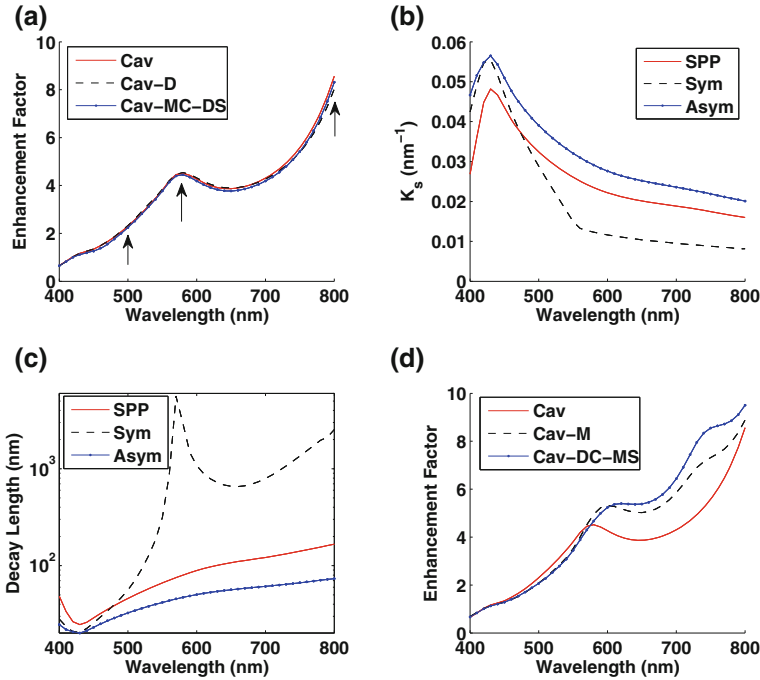


**Fig. 7.11** **a** The spectral enhancement factors for the plasmonic cavity (Cav) and for that coupled with the dielectric (D) or the metal-core dielectric-shell (MC-DS) sphere; **b** the dispersion relations of surface plasmon polariton (SPP), and a symmetric (Sym) and asymmetric (Asym) surface wave modes. The surface plasmon polariton propagates at the interface between semi-infinite polymer and Ag half-spaces. The symmetric and asymmetric modes propagate in the active polymer layer bounded between the two metal claddings with finite thicknesses; **c** the decay lengths penetrated into the active material; **d** the spectral enhancement factors for the plasmonic cavity and for that coupled with the metal (M) or the dielectric-core metal-shell (DC-MS) sphere. ©2011 OSA; Ref. [33]

has a good overlap with the absorption spectrum of the active material as depicted in Fig. 7.10a. The dispersion relation of the cavity resonator plays a key role in unveiling the fundamental physics of the significant optical enhancement. Different from previous works assuming infinitely thick metal claddings [86], we take into account the finite-thickness effect of the metal claddings. The governing equation for the 1D eigenvalue problem of the Air/Ag/polymer/Ag/Air planar layered media is given by [59]

$$\left[ p \frac{d}{dx} p^{-1} \frac{d}{dx} + K^2(x) \right] \phi(x) = K_z^2 \phi(x) \quad (7.47)$$

where  $p = \varepsilon$  and  $\phi = H_y$  for TM wave, and  $p = \mu$  and  $\phi = E_y$  for TE wave. The eigenvalue equation (7.47) can be easily solved by the FDFD method with perfectly matched layer absorbing boundary conditions presented in Sect. 7.3.2. We

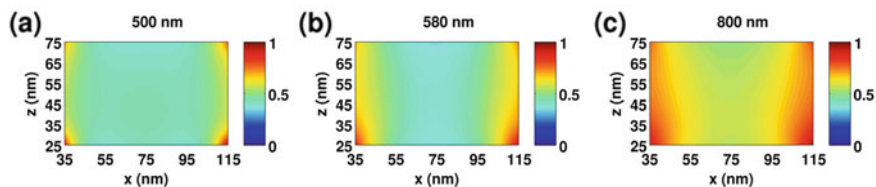


**Fig. 7.12** The near-field distributions in the active polymer layer at the wavelengths denoted with the arrows of Fig. 7.11a: **a** 500 nm; **b** 580 nm; **c** 800 nm. ©2011 OSA; Ref. [33]

find two eigenvalues of the TM wave closest to the momentum of surface plasmon polariton (SPP). The SPP propagates at the interface between semi-infinite polymer and Ag half spaces and its dispersion relation is of the form

$$K_z = K_0 \sqrt{\frac{\varepsilon_{\text{Ag}} \varepsilon_{\text{pol}}}{\varepsilon_{\text{Ag}} + \varepsilon_{\text{pol}}}} \quad (7.48)$$

Particularly, the eigenvalue pair essentially corresponds to the symmetric and asymmetric surface wave modes supported by the Ag/polymer/Ag system [40, 86]. These modes are also associated with the guided-wave poles of the generalized reflection coefficient for the planar layered media [59]. Figure 7.11b shows the dispersion relations. At long wavelengths, the dispersion relation of the SPP is located between those of symmetric and asymmetric modes. Then we calculate the decay lengths of the surface plasmon waves penetrated into the active material as plotted in Fig. 7.11c. The peaks of the decay length of the symmetric mode strongly coincide with those of the spectral enhancement factor as shown in Fig. 7.11a. The incident light excites symmetric surface plasmon waves at the bottom corners of the cavity and the waves propagate in the active layer bounded between the metal claddings. A short decay length away from the metal claddings makes  $E$ -fields concentrate at the surfaces of the metals. Contrarily, a long decay length induces a concentrated  $E$ -field in the center of the active material. Figure 7.12 demonstrates the near-field distributions in the active layer at the wavelengths denoted with the arrows of Fig. 7.11a. At 800 nm, the slowly decaying near field away from the metal claddings leads to the most significant enhancement.

Third, we study the hybrid plasmonic system, which comprises a plasmonic cavity coupled with a nanosphere. The optical enhancement shows little improvements when the cavity is coupled with the dielectric or MC-DS sphere as illustrated in Fig. 7.11a. However, a significant enhancement can be achieved if the cavity is coupled with metal or DC-MS sphere as shown in Fig. 7.11d. Employing the cavity coupled with the DC-MS sphere, the optical absorption of the active polymer material has a 4-fold increase according to the obtained total enhancement factor (defined in Sect. 7.3.4). We calculate the algebraic summation of the spectral enhancement factor by the uncoupled single cavity and that by the uncoupled single DC-MS sphere. As shown in Fig. 7.13, the summation is

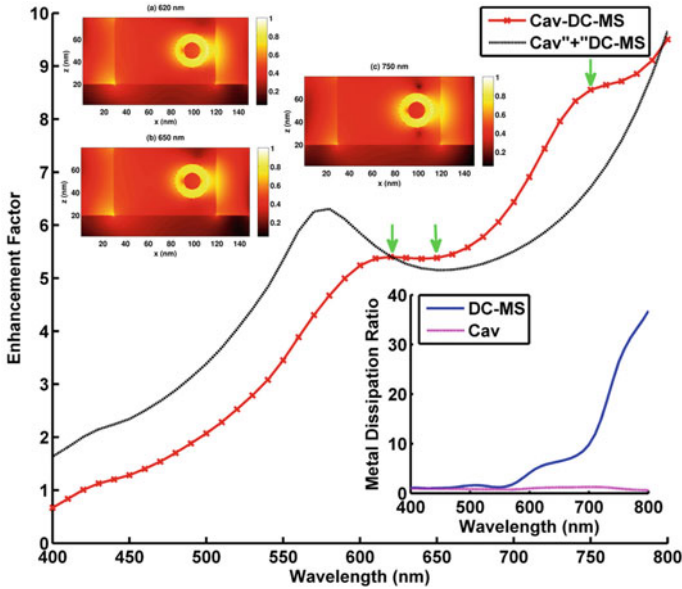
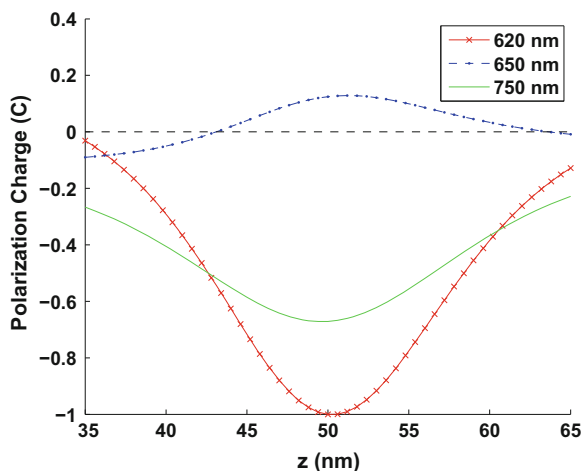


**Fig. 7.13** The spectral enhancement factor comparisons. The enhancement factor by the cavity (Cav) coupled with the DC-MS sphere is drawn with *red straight line*. The algebraic summation of the enhancement factor by the uncoupled single cavity and that by the uncoupled single DC-MS sphere is plotted with *black dash line*. The near-field distributions at the wavelengths denoted with the *green arrows* are shown in the *inset*. The metal dissipation ratio of the cavity is defined as the metal loss of the coupled cavity over that of the uncoupled one. Likewise, the metal dissipation ratio of the DC-MS sphere is defined as the metal loss of the coupled DC-MS sphere over that of the uncoupled one. ©2011 OSA; Ref. [33]

observably smaller than the enhancement factor by the cavity coupled with the DC-MS sphere at long wavelengths ranging from 620 to 800 nm. The coherent interplay between the cavity and the DC-MS sphere is undoubtedly confirmed by the result. Then, we analyze the metal dissipation ratio defined as the metal loss of the coupled concentrator over that of the uncoupled one. The inset of Fig. 7.13 shows that the metal dissipation ratio of the DC-MS sphere is substantially larger than that of the cavity. The evanescent SPPs from the inner surface of metallic cavity sufficiently penetrate the DC-MS sphere inducing stronger local plasmon resonance as well as larger metallic loss. Thus, the DC-MS sphere becomes more effective concentrator when it is coupled with the cavity. Finally, we discuss the coupling modes in the hybrid plasmonic system. Calculated by Eq. (7.37), Fig. 7.14 depicts a polarization charge distribution on the surface of the cavity, indicating a bonding and antibonding coupling modes in the hybrid system. The bonding modes at 620 and 750 nm have a denser charge distribution if the distance between the cavity and the shell surfaces becomes closer. However, the antibonding mode at 650 nm reverses the polarity of the polarization charge when the face-to-face distance approaches the minimum. The near fields of the bonding

**Fig. 7.14** The polarization charge distributions on the surface of the cavity at the wavelengths denoted with the arrows of Fig. 7.13. ©2011 OSA; Ref. [33]



modes show more concentrated field at the gap between the DC-MS sphere and the cavity, which can be seen in the inset of Fig. 7.13. For the bonding mode, the polarity of its polarization charge is marked in Fig. 7.9. Due to the in-phase plasmon oscillation and hybridization, the bonding mode is superradiant or strongly radiative, and provides a great help for the optical enhancement.

In conclusion, the hybrid plasmonic system, which comprises the plasmonic cavity coupled with the DC-MS nanosphere, can increase the optical absorption of the OSC by fourfold. The significant enhancement mainly results from the coupling of symmetric surface wave modes supported by the cavity resonator and strongly depends on the decay length of surface plasmon waves penetrated into the active layer. Furthermore, the coherent interplay between the cavity and the DC-MS nanosphere is strongly demonstrated by our theoretical model. The bonding coupling mode in the hybrid plasmonic system enhances the optical absorption further. The work provides detailed physical explanations for the hybrid plasmonic cavity device structure to enhance the optical absorption of organic photovoltaics.

## 7.5 Conclusion

In this book chapter, we have reviewed the basic concepts, physical mechanisms, and theoretical models for plasmonic effects in OSCs. Our results show that the absorption and performance of OSCs can be significantly enhanced by incorporating metallic nanostructures. The unparalleled near-field concentration inherent from plasmon resonances can break the half-wavelength limit in the optical design of thin-film OSCs, which is particularly useful for high-performance ultracompact photovoltaics.

We can explore new potentials and emerging functionalities of plasmonic effects in OSCs. On the one hand, the bad spectral overlap of plasmonic resonances with the absorption of active polymer materials could be improved by plasmonic hybridization or by combination with high-refractive-index materials. On the other hand, the electrical properties of plasmonic nanostructures and resulting effects can be investigated with multiphysics study.

**Acknowledgments** The authors acknowledge the support of the grants (Nos. 712010, 711609, and 711511) from the Research Grant Council (RGC) of Hong Kong, the grant (No. 10401466) from the University Grant Council (UGC) of the University of Hong Kong, and the Small Project Funding of the University of Hong Kong (No. 201109176133). This project is also supported by the UGC of Hong Kong (No. AoE/P-04/08), by The National Natural Science Foundation of China (No. 61201122), and in part by a Hong Kong UGC Special Equipment Grant (SEG HKU09).

## Appendix—Biconjugate Gradient Stabilized Algorithm

The resulting VIE matrix equation can be expressed as

$$Ax = b$$

The procedure of the biconjugate gradient stabilized (BI-CGSTAB) algorithm is given as follows:

Give an initial guess  $x_0$ , we have

$$\begin{aligned} r_0 &= b - Ax_0, \hat{r}_0 = r_0 \\ \rho_0 &= \alpha = \omega_0 = 1 \\ v_0 &= p_0 = 0 \end{aligned}$$

Iterate for  $i = 1, 2, \dots, n$

$$\begin{aligned} \rho_i &= \langle \hat{r}_0, r_{i-1} \rangle \\ \beta &= (\rho_i / \rho_{i-1})(\alpha / \omega_{i-1}) \\ p_i &= r_{i-1} + \beta(p_{i-1} - \omega_{i-1}v_{i-1}) \\ v_i &= Ap_i \\ \alpha &= \rho_i / \langle \hat{r}_0, v_i \rangle \\ s &= r_{i-1} - \alpha v_i \\ t &= As \\ \omega_i &= \langle t, s \rangle / \langle t, t \rangle \\ x_i &= x_{i-1} + \alpha p_i + \omega_i s \\ r_i &= s - \omega_i t \end{aligned}$$

Terminate when

$$\frac{\|r_i\|_2}{\|b\|_2} < \eta$$

where  $\eta$  is the tolerance that specifies the desired accuracy of solution.

## References

1. Hoppe H, Sariciftci NS (2004) Organic solar cells: an overview. *J Mater Res* 19:1924–1945
2. Brabec CJ, Gowrisanker S, Halls JJM, Laird D, Jia SJ, Williams SP (2010) Polymer-fullerene bulk-heterojunction solar cells. *Adv Mater* 22:3839–3856
3. Deibel C, Dyakonov V (2010) Polymer-fullerene bulk heterojunction solar cells. *Rep Prog Phys* 73:096401
4. Barnes WL, Dereux A, Ebbesen TW (2003) Surface plasmon subwavelength optics. *Nature* 424:824–830
5. Gramotnev DK, Bozhevolnyi SI (2010) Plasmonics beyond the diffraction limit. *Nat Photonics* 4:83–91
6. Schuller JA, Barnard ES, Cai WS, Jun YC, White JS, Brongersma ML (2010) Plasmonics for extreme light concentration and manipulation. *Nat Mater* 9:193–204
7. Atwater HA, Polman A (2010) Plasmonics for improved photovoltaic devices. *Nat Mater* 9:205–213
8. Tvingstedt K, Persson NK, Inganäs O, Rahachou A, Zozoulenko IV (2007) Surface plasmon increase absorption in polymer photovoltaic cells. *Appl Phys Lett* 91:113514
9. Bai WL, Gan QQ, Bartoli F, Zhang J, Cai LK, Huang YD, Song GF (2009) Design of plasmonic back structures for efficiency enhancement of thin-film amorphous Si solar cells. *Opt Lett* 34:3725–3727
10. Bai WL, Gan QQ, Song GF, Chen LH, Kafafi Z, Bartoli F (2010) Broadband short-range surface plasmon structures for absorption enhancement in organic photovoltaics. *Opt Express* 18:A620–A630
11. Kang MG, Xu T, Park HJ, Luo XG, Guo LJ (2010) Efficiency enhancement of organic solar cells using transparent plasmonic Ag nanowire electrodes. *Adv Mater* 22:4378–4383
12. Min CJ, Li J, Veronis G, Lee JY, Fan SH, Peumans P (2010) Enhancement of optical absorption in thin-film organic solar cells through the excitation of plasmonic modes in metallic gratings. *Appl Phys Lett* 96:133302
13. Tsai SJ, Ballarotto M, Romero DB, Herman WN, Kan HC, Phaneuf RJ (2010) Effect of gold nanopillar arrays on the absorption spectrum of a bulk heterojunction organic solar cell. *Opt Express* 18:A528–A535
14. Wang W, Wu SM, Reinhardt K, Lu YL, Chen SC (2010) Broadband light absorption enhancement in thin-film silicon solar cells. *Nano Lett* 10:2012–2018
15. Sha WEI, Choy WCH, Chew WC (2010) A comprehensive study for the plasmonic thin-film solar cell with periodic structure. *Opt Express* 18:5993–6007
16. Sha WEI, Choy WCH, Chew WC (2011) Angular response of thin-film organic solar cells with periodic metal back nanostrips. *Opt Lett* 36:478–480
17. Sha WEI, Choy WCH, Wu Y, Chew WC (2012) Optical and electrical study of organic solar cells with a 2D grating anode. *Opt Express* 20:2572–2580
18. Catchpole KR, Polman A (2008) Plasmonic solar cells. *Opt Express* 16:21793–21800
19. Catchpole KR, Polman A (2008) Design principles for particle plasmon enhanced solar cells. *Appl Phys Lett* 93:191113

20. Morfa AJ, Rowlen KL, Reilly TH, Romero MJ, van de Lagemaat J (2008) Plasmon-enhanced solar energy conversion in organic bulk heterojunction photovoltaics. *Appl Phys Lett* 92:013504
21. Duche D, Torchio P, Escoubas L, Monestier F, Simon JJ, Flory F, Mathian G (2009) Improving light absorption in organic solar cells by plasmonic contribution. *Sol Energy Mater Sol Cells* 93:1377–1382
22. Mendes MJ, Luque A, Tobias I, Marti A (2009) Plasmonic light enhancement in the near-field of metallic nanospheroids for application in intermediate band solar cells. *Appl Phys Lett* 95:071105
23. Akimov YA, Koh WS, Ostrikov K (2009) Enhancement of optical absorption in thin-film solar cells through the excitation of higher-order nanoparticle plasmon modes. *Opt Express* 17:10195–10205
24. Akimov YA, Ostrikov K, Li EP (2009) Surface plasmon enhancement of optical absorption in thin-film silicon solar cells. *Plasmonics* 4:107–113
25. Mokkapatil S, Beck FJ, Polman A, Catchpole KR (2009) Designing periodic arrays of metal nanoparticles for light-trapping applications in solar cells. *Appl Phys Lett* 95:053115
26. Lee JY, Peumans P (2010) The origin of enhanced optical absorption in solar cells with metal nanoparticles embedded in the active layer. *Opt Express* 18:10078–10087
27. Kulkarni AP, Noone KM, Munchika K, Guyer SR, Ginger DS (2010) Plasmon-enhanced charge carrier generation in organic photovoltaic films using silver nanoparticles. *Nano Lett* 10:1501–1505
28. Jung J, Sondergaard T, Pedersen TG, Pedersen K, Larsen AN, Nielsen BB (2011) Dyadic Green's functions of thin films: applications within plasmonic solar cells. *Phys Rev B* 83:085419
29. Diukman I, Tzabari L, Berkovitch N, Tessler N, Orenstein M (2011) Controlling absorption enhancement in organic photovoltaic cells by patterning Au nano disks within the active layer. *Opt Express* 19:A64–A71
30. Sha WEI, Choy WCH, Liu YG, Chew WC (2011) Near-field multiple scattering effects of plasmonic nanospheres embedded into thin-film organic solar cells. *Appl Phys Lett* 99:113304
31. Ferry VE, Sweatlock LA, Pacifici D, Atwater HA (2008) Plasmonic nanostructure design for efficient light coupling into solar cells. *Nano Lett* 8:4391–4397
32. Pala RA, White J, Barnard E, Liu J, Brongersma ML (2009) Design of plasmonic thin-film solar cells with broadband absorption enhancements. *Adv Mater* 21:3504–3509
33. Sha WEI, Choy WCH, Chen YP, Chew WC (2011) Optical design of organic solar cell with hybrid plasmonic system. *Opt Express* 19:15908–15918
34. Chopra KL, Paulson PD, Dutta V (2004) Thin-film solar cells: an overview. *Prog Photovoltaics* 12:69–92
35. Tikhodeev SG, Yablonskii AL, Muljarov EA, Gippius NA, Ishihara T (2002) Quasiguidded modes and optical properties of photonic crystal slabs. *Phys Rev B* 66:045102
36. Hessel A, Oliner AA (1965) A new theory of Wood's anomalies on optical gratings. *Appl Optics* 4:1275–1297
37. Luk'yanchuk B, Zheludev NI, Maier SA, Halas NJ, Nordlander P, Giessen H, Chong CT (2010) The Fano resonance in plasmonic nanostructures and metamaterials. *Nat Mater* 9:707–715
38. Miroshnichenko AE, Flach S, Kivshar YS (2010) Fano resonances in nanoscale structures. *Rev Mod Phys* 82:2257–2298
39. Raether H (1988) *Surface plasmons on smooth and rough surfaces and on gratings*. Springer, Berlin
40. Maier SA (2007) *Plasmonics: fundamentals and applications*. Springer, New York
41. Kawata S, Shalaev VM (2007) *Nanophotonics with surface plasmons*. Elsevier, Amsterdam
42. Prodan E, Radloff C, Halas NJ, Nordlander P (2003) A hybridization model for the plasmon response of complex nanostructures. *Science* 302:419–422



43. Nordlander P, Oubre C, Prodan E, Li K, Stockman MI (2004) Plasmon hybridization in nanoparticle dimers. *Nano Lett* 4:899–903
44. Matheu P, Lim SH, Derkacs D, McPheeters C, Yu ET (2008) Metal and dielectric nanoparticle scattering for improved optical absorption in photovoltaic devices. *Appl Phys Lett* 93:113108
45. Akimov YA, Koh WS, Sian SY, Ren S (2010) Nanoparticle-enhanced thin film solar cells: metallic or dielectric nanoparticles? *Appl Phys Lett* 96:073111
46. Grandidier J, Callahan DM, Munday JN, Atwater HA (2011) Light absorption enhancement in thin-film solar cells using whispering gallery modes in dielectric nanospheres. *Adv Mater* 23:1272–1276
47. Giannini V, Fernandez-Dominguez AI, Sonnefraud Y, Roschuk T, Fernandez-Garcia R, Maier SA (2010) Controlling light localization and light-matter interactions with nanoplasmonics. *Small* 6:2498–2507
48. Chew WC, Jin J-M, Michielssen E, Song J (2001) *Fast and efficient algorithms in computational electromagnetics*. Artech House Publishers, Boston
49. Luebbers R, Hunsberger FP, Kunz KS, Standler RB, Schneider M (1990) A frequency-dependent finite-difference time-domain formulation for dispersive materials. *IEEE Trans Electromagn Compat* 32:222–227
50. Kelley DF, Luebbers RJ (1996) Piecewise linear recursive convolution for dispersive media using FDTD. *IEEE Trans Antennas Propag* 44:792–797
51. Veronis G, Fan S (2007) Overview of simulation techniques for plasmonic devices. In: Brongersma ML, Kik PG (eds) *Surface plasmon nanophotonics*. Springer, Dordrecht
52. Veysoglu ME, Shin RT, Kong JA (1993) A finite-difference time-domain analysis of wave scattering from periodic surfaces-oblique-incidence case. *J Electromagn Waves Appl* 7:1595–1607
53. Sullivan DM (2000) *Electromagnetic simulation using the FDTD method*. Wiley-IEEE Press, New York
54. Taflove A, Hagness SC (2005) *Computational electrodynamics: the finite-difference time-domain method*, 3rd edn. Artech House, Boston
55. Jin J-M (2002) *The finite element method in electromagnetics*, 2nd edn. Wiley-IEEE Press, New York
56. Chew WC, Tong MS, Hu B (2008) *Integral equation methods for electromagnetic and elastic waves*. Morgan and Claypool Publishers, San Rafael
57. Brandt A (1982) *Guide to multigrid development*. Lecture notes in mathematics, vol 960, pp 220–312
58. Davis TA, Duff IS (1997) An unsymmetric-pattern multifrontal method for sparse LU factorization. *SIAM J Matrix Anal Appl* 18:140–158
59. Chew WC (1995) *Waves and fields in inhomogenous media*. Wiley-IEEE Press, New York
60. Chew WC, Jin JM, Lu CC, Michielssen E, Song JMM (1997) Fast solution methods in electromagnetics. *IEEE Trans Antennas Propag* 45:533–543
61. Brandt A (1991) Multilevel computations of integral-transforms and particle interactions with oscillatory kernels. *Comput Phys Commun* 65:24–38
62. Phillips JR, White JK (1997) A precorrected-FFT method for electrostatic analysis of complicated 3-D structures. *IEEE Trans Comput-Aided Des Integr Circuits Syst* 16:1059–1072
63. Greengard L, Rokhlin V (1987) A fast algorithm for particle simulations. *J Comput Phys* 73:325–348
64. Song JM, Lu CC, Chew WC (1997) Multilevel fast multipole algorithm for electromagnetic scattering by large complex objects. *IEEE Trans Antennas Propag* 45:1488–1493
65. Bienstman P, Baets R (2001) Optical modelling of photonic crystals and VCSELs using eigenmode expansion and perfectly matched layers. *Opt Quantum Electron* 33:327–341
66. Moharam MG, Grann EB, Pommet DA, Gaylord TK (1995) Formulation for stable and efficient implementation of the rigorous coupled-wave analysis of binary gratings. *J Opt Soc Am A* 12:1068–1076

67. Yonekura J, Ikeda M, Baba T (1999) Analysis of finite 2-D photonic crystals of columns and lightwave devices using the scattering matrix method. *J Lightwave Technol* 17:1500–1508
68. Johnson SG, Joannopoulos JD (2001) Block-iterative frequency-domain methods for Maxwell's equations in a planewave basis. *Opt Express* 8:173–190
69. Yee KS (1966) Numerical solution of initial boundary value problems involving Maxwell's equations in isotropic media. *IEEE Trans Antennas Propag* 14:302–307
70. Berenger JP (1994) A perfectly matched layer for the absorption of electromagnetic-waves. *J Comput Phys* 114:185–200
71. Chew WC, Weedon WH (1994) A 3-D perfectly matched medium from modified Maxwell's equations with stretched coordinates. *Microw Opt Technol Lett* 7:599–604
72. Mur G (1981) Absorbing boundary-conditions for the finite-difference approximation of the time-domain electromagnetic-field equations. *IEEE Trans Electromagn Compat* 23:377–382
73. Draine BT, Flatau PJ (1994) Discrete-dipole approximation for scattering calculations. *J Opt Soc Am A* 11:1491–1499
74. Kern AM, Martin OJF (2009) Surface integral formulation for 3D simulations of plasmonic and high permittivity nanostructures. *J Opt Soc Am A* 26:732–740
75. Glisson AW, Wilton DR (1980) Simple and efficient numerical methods for problems of electromagnetic radiation and scattering from surfaces. *IEEE Trans Antennas Propag* 28:593–603
76. Catedra MF, Gago E, Nuno L (1989) A numerical scheme to obtain the RCS of three-dimensional bodies of resonant size using the conjugate gradient method and the fast Fourier transform. *IEEE Trans Antennas Propag* 37:528–537
77. Hestenes MR, Stiefel E (1952) Methods of conjugate gradients for solving linear systems. *J Res Nat Bur Stand* 49:409–436
78. Vandervorst HA (1992) Bi-CGSTAB: a fast and smoothly converging variant of Bi-CG for the solution of nonsymmetric linear systems. *SIAM J Sci Stat Comput* 13:631–644
79. Bohren CF, Huffman DR (1998) Absorption and scattering of light by small particles. Wiley-Interscience, New York
80. Tsang L, Kong JA, Ding KH (2000) Scattering of electromagnetic waves: theories and applications. Wiley, New York
81. Rakic AD, Djuricic AB, Elazar JM, Majewski ML (1998) Optical properties of metallic films for vertical-cavity optoelectronic devices. *Appl Optics* 37:5271–5283
82. Palik ED (1998) Handbook of optical constants of solids. Academic Press, London
83. Choy WCH, Fong HH (2008) Comprehensive investigation of absolute optical properties of organic materials. *J Phys D Appl Phys* 41:155109
84. Wei QH, Su KH, Durant S, Zhang X (2004) Plasmon resonance of finite one-dimensional Au nanoparticle chains. *Nano Lett* 4:1067–1071
85. Jain PK, El-Sayed MA (2007) Universal scaling of plasmon coupling in metal nanostructures: extension from particle pairs to nanoshells. *Nano Lett* 7:2854–2858
86. Prade B, Vinet JY, Mysyrowicz A (1991) Guided optical waves in planar heterostructures with negative dielectric-constant. *Phys Rev B* 44:13556–13572